chemosensors

MDPI

Article

Electrostatic Self-Assembly of Heterostructured $In_2O_3/Ti_3C_2T_x$ Nanocomposite for High-Selectivity NO_2 Gas Sensing at Room Temperature

Yongjing Guo [1], Zhengxin Zhang [1], Hangshuo Feng [1], Qingfu Dai [1], Qiuni Zhao [1,*], Zaihua Duan [2], Shenghui Guo [1,*], Li Yang [1], Ming Hou [1] and Yi Xia [1,*]

[1] Faculty of Metallurgical and Energy Engineering, Kunming University of Science and Technology, Kunming 650093, China; guoyongjing98@163.com (Y.G.); zhangzhengxin2024@163.com (Z.Z.); hangshuofeng2002@163.com (H.F.); daiqingfu0077@163.com (Q.D.); yanglikmust@163.com (L.Y.); houmingkmust@163.com (M.H.)

[2] State Key Laboratory of Electronic Thin Films and Integrated Devices, School of Optoelectronic Science and Engineering, University of Electronic Science and Technology of China (UESTC), Chengdu 611731, China; zaihuaduan@uestc.edu.cn

* Correspondence: qiunizhao90s@163.com (Q.Z.); 20040051@kust.edu.cn (S.G.); xiayi0125@163.com (Y.X.)

Abstract

Owing to high electrical conductivity, layered structure, and abundant surface functional groups, transition metal carbides/nitrides (MXenes) have received enormous interest in the field of gas sensors at room temperature. In this work, we synthesize a heterostructured nanocomposite with indium oxide (In_2O_3) decorated on titanium carbide ($Ti_3C_2T_x$) nanosheets by electrostatic self-assembly and develop it for high-selectivity NO_2 gas sensing at room temperature. Self-assembly formation of multiple heterojunctions in the $In_2O_3/Ti_3C_2T_x$ composite provide abundant NO_2 gas adsorption sites and high electron transfer activity, which is conducive to improving the gas-sensing response of the $In_2O_3/Ti_3C_2T_x$ gas sensor. Assisted by rich adsorption sites and hetero interface, the as-fabricated $In_2O_3/Ti_3C_2T_x$ gas sensor exhibits the highest response to NO_2 among various interference gases. Meanwhile, a detection limit of 0.3 ppm, and response/recovery time (197.62/93.84 s) is displayed at room temperature. Finally, a NO_2 sensing mechanism of $In_2O_3/Ti_3C_2T_x$ gas sensor is constructed based on PN heterojunction enhancement and molecular adsorption. This work not only expands the gas-sensing application of MXenes, but also demonstrates an avenue for the rational design and construction of NO_2-sensing materials.

Keywords: MXene; $Ti_3C_2T_x$; In_2O_3; gas sensing; heterostructure; electrostatic self-assembly

check for updates

Received: 6 June 2025
Revised: 28 June 2025
Accepted: 8 July 2025
Published: 10 July 2025

Citation: Guo, Y.; Zhang, Z.; Feng, H.; Dai, Q.; Zhao, Q.; Duan, Z.; Guo, S.; Yang, L.; Hou, M.; Xia, Y. Electrostatic Self-Assembly of Heterostructured $In_2O_3/Ti_3C_2T_x$ Nanocomposite for High-Selectivity NO_2 Gas Sensing at Room Temperature. *Chemosensors* **2025**, *13*, 249. https://doi.org/10.3390/chemosensors13070249

Copyright: © 2025 by the authors. Licensee MDPI, Basel, Switzerland. This article is an open access article distributed under the terms and conditions of the Creative Commons Attribution (CC BY) license (https://creativecommons.org/licenses/by/4.0/).

1. Introduction

With the development of global industrialization, atmospheric pollutants in the ecological environment have greatly restricted the development of social economy and become a serious problem for contemporary civilization [1–3]. Nitrogen dioxide (NO_2), as a hazardous gas, is harmful to human health when its concentration exceeds 3 ppm [4,5]. Therefore, developing fast, highly sensitive, and highly selective NO_2 gas sensors is crucial for protecting human health and monitoring the atmospheric environment [6–8].

Among numerous gas detection technologies, metal oxide semiconductor (MOS)-based gas sensors are widely used due to their advantages of low cost, small size, easy integration, and real-time monitoring [9–12]. Metal oxide-based gas-sensing materials

mainly include tin dioxide (SnO_2), zinc oxide (ZnO), tungsten trioxide (WO_3), indium oxide (In_2O_3), and copper oxide (CuO) [13–16]. Among them, In_2O_3 is widely used in the manufacture of gas sensors due to its high sensitivity and fast response characteristics [17,18]. For instance, Zhang et al. [19], using the electrospinning method, prepared In_2O_3 nanowires for NO_2 gas sensing under visible light irradiation (400–700 nm, 4.58 $mW \cdot cm^{-2}$). The In_2O_3 nanowire-based NO_2 gas sensor exhibits a response value of 780 to 5 ppm NO_2, with a response and recovery time of 200 s and 20 s, respectively. Most MOS-based gas sensors demand either elevated operating temperatures or light irradiation, leading to higher power consumption. Meanwhile, this type of sensor displays a broad-spectrum response to multiple gases (such as NO_2, ammonia (NH_3), hydrogen sulfide (H_2S), sulfur dioxide (SO_2), and volatile organic compounds (VOCs)), which leads to the insufficient selectivity of MOS-based gas sensors [20,21].

Two-dimensional (2D) materials (such as graphene, transition-metal dichalcogenides (TMDs), graphitic carbon nitride (g-C_3N_4)) have received tremendous attention as gas-sensing materials in recent years due to their high specific surface area, rich surface chemical bond, atomic-level thickness, and adjustable electrical properties. MXene is a group of transition metal carbides/nitrides/carbonitrides with a layered structure, discovered by Gogosti in 2011 [22]. Most MXene, such as titanium carbide ($Ti_3C_2T_x$), vanadium carbide (V_2CT_x), and niobium carbide (Nb_2CT_x), is synthesized by the selective etching out of the A layers from MAX phases, where A is mainly a group IIIA or IVA element, M represents an early transition metal, and X is carbon and/or nitrogen [23,24]. Thus, the surface of MXene is rich in defects, and the functional groups on its surface can be regulated by selecting the synthesis method [25]. In addition, the layered structure of MXene will provide abundant active sites for gas adsorption and surface reactions, and high carrier mobility of MXene is beneficial for reducing the signal noise of the gas sensors [26,27]. However, MXene-based gas-sensitive materials mainly suffer from oxidation by NO_2, which leads to poor stability of the NO_2 gas sensor due to MXene deterioration. Thus, forming a protective film on the surface of MXene by modification or composite is a common strategy to improve the stability of MXene. Classically, $Ti_3C_2T_x/TiO_2$ nanocomposite are prepared by in situ growth, formation of Schottky barrier can effectively improve the performance of $Ti_3C_2T_x$-based NO_2 gas sensors [28,29].

In this work, we investigated the achievement of decorating In_2O_3 on $Ti_3C_2T_x$ nanosheets via electrostatic self-assembly to enhance gas-sensing response at room temperature. The morphology and chemical structure of composite are characterized, and the gas-sensing performances of $In_2O_3/Ti_3C_2T_x$ gas sensors are investigated in this study. The formation of multiple heterojunctions in the $In_2O_3/Ti_3C_2T_x$ composite provide abundant NO_2 gas adsorption sites and high electron transfer activity, resulting in high response and selectivity of the $In_2O_3/Ti_3C_2T_x$ gas sensor. Moreover, the enhanced NO_2 gas-sensing mechanism is demonstrated based on heterojunction and molecular adsorption. This work expands the application of MXene in the field of gas sensor.

2. Materials and Methods

2.1. Sample Preparation

The reagents used in this study were purchased through standard commercial channels without further modification. Indium nitrate pentahydrate ($In(NO_3)_3 \cdot 5H_2O$), N, N-dimethylformamide (C_3H_7NO, DMF), urea (CH_4N_2O), lithium fluoride (LiF), hydrochloric acid (HCl), poly(diallyldimethylammonium chloride) (PDDA), and methanol were purchased from Shanghai Macklin Biochemical Technology Co., Ltd. (Shanghai, China). Titanium aluminum carbide (Ti_3AlC_2) was bought from Jilin 11 Technology Co., Ltd.

(Changchun, Jilin, China). In this study, the $In_2O_3/Ti_3C_2T_x$ composite was synthesized using hydrothermal and electrostatic self-assembly methods, as illustrated in Figure 1.

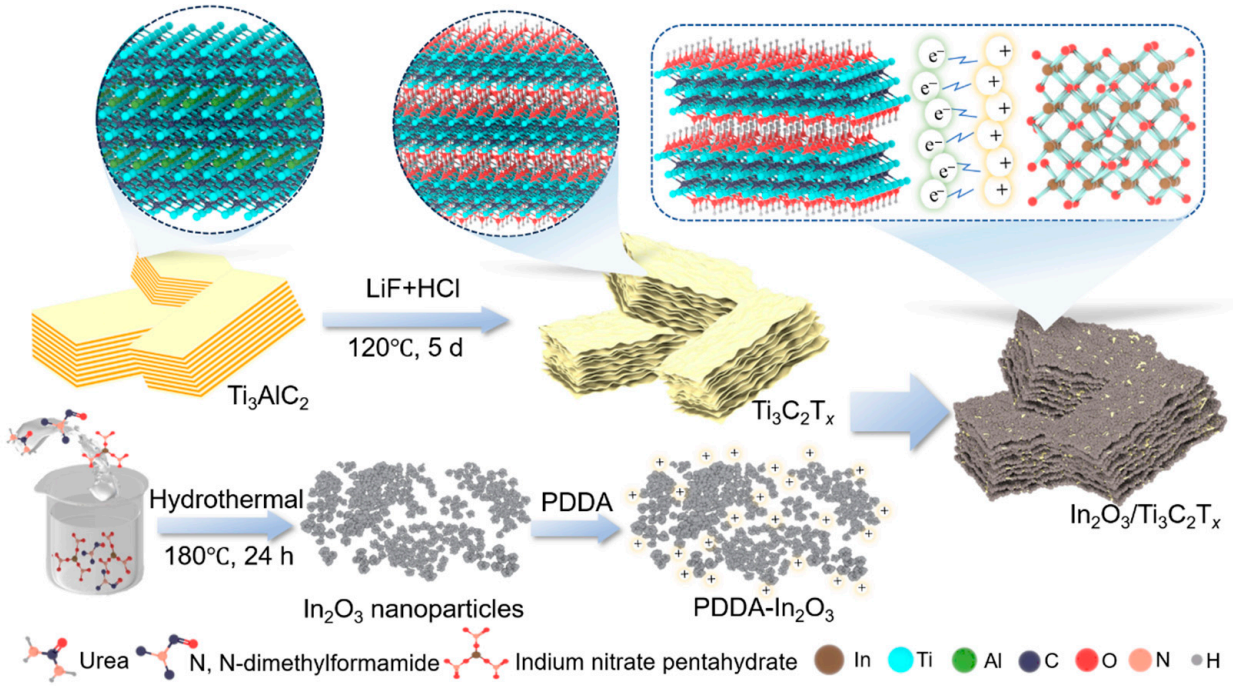


Figure 1. Schematic illustration of the synthesis of the $In_2O_3/Ti_3C_2T_x$ composite.

(1) Synthesis of zero-dimensional In_2O_3 nanoparticles

The In_2O_3 nanoparticles were synthesized using the hydrothermal method [30]. Initially, 0.5 mmol ($In(NO_3)_3 \cdot 5H_2O$) was dissolved in 20 mL DMF. Subsequently, 0.01 mol urea was added to the solution and stirred for 1 h until the solution becomes transparent. The solution was transferred to a 25 mL polytetrafluoroethylene-lined autoclave and hydrothermally treated at 180 °C for 24 h. Upon completion of the reaction, a white precipitate was obtained, which was repeatedly washed multiple times via centrifugation using deionized water and ethanol. The washed product then dried in a vacuum oven at 60 °C for 12 h. After drying, the sample was placed in a tubular furnace and calcined at 500 °C for 2 h to obtain In_2O_3 nanoparticles.

(2) Synthesis of 2D $Ti_3C_2T_x$

A 1.3 g measurement of LiF powder was dissolved in 80 mL hydrochloric acid (6 $mol \cdot L^{-1}$) and stirred at room temperature for 30 min. Then 2 g Ti_3AlC_2 was added slowly, and the mixture was stirred for an additional 30 min. The resulting solution was transferred to a 150 mL polytetrafluoroethylene-lined autoclave and heated in a constant-temperature oven at 120 °C for 5 days. After the reaction was completed, the autoclave was cooled to room temperature and taken out. The obtained precipitate was repeatedly centrifuged and washed several times with deionized water and ethanol until the pH was close to 7 and then placed in a 60 °C vacuum drying oven for drying to obtain black $Ti_3C_2T_x$ powder.

(3) Synthesis of $In_2O_3/Ti_3C_2T_x$ Composite

The $In_2O_3/Ti_3C_2T_x$ composite was synthesized via electrostatic self-assembly. Firstly, 1 g In_2O_3 nanoparticles was dispersed in 300 mL of 0.5 wt% PDDA solution and ultrasonic treatment for 3 h. Following filtration, the PDDA-modified In_2O_3 was rinsed with deionized water and dried in a drying oven at 70 °C for 12 h. Subsequently, 1 g of the

PDDA-modified In_2O_3 powder was dispersed in 10 mL methanol. $Ti_3C_2T_x$ with different mass (10 mg, 20 mg, and 50 mg) was added to the solution, and the mixture was stirred vigorously for 10 h. Finally, the suspension was washed with methanol several times and dried in a vacuum oven at 70 °C for 12 h to obtain the $In_2O_3/Ti_3C_2T_x$ composite. For the convenience of description, the different $In_2O_3/Ti_3C_2T_x$ composites are designated as IT1, IT2, and IT3, with $Ti_3C_2T_x$ proportions of 1%, 2%, and 5%, respectively. The performance of the optimized IT2 is consistently referred to as $In_2O_3/Ti_3C_2T_x$ composite in subsequent sections.

2.2. Characterization Method

The crystalline phase of the $In_2O_3/Ti_3C_2T_x$ composite was analyzed by X-ray diffraction (XRD, Rigaku D/max-2500, Rigaku, Tokyo, Japan). The microstructure of $In_2O_3/Ti_3C_2T_x$ composite was characterized by field emission scanning electron microscopy (FESEM JSM-7100F, JEOL, Tokyo, Japan) and high-resolution transmission electron microscopy (HRTEM, Tecnai G2 F30-S-Twin, FEI, Hillsboro, OR, USA). The EDS spectrum of $In_2O_3/Ti_3C_2T_x$ composite was obtained by energy dispersive spectrometer (EDS, Hitachi S-4800, Hitachi, Tokyo, Japan). The different elemental compositions and chemical states of $In_2O_3/Ti_3C_2T_x$ composite were analyzed by scanning imaging photoelectron spectroscopy (XPS, PHI5000 Versaprobe-II, ULVAC-PHI, Tokyo, Japan). The direct band gap energy of In_2O_3 and $In_2O_3/Ti_3C_2T_x$ composite was obtained by UV-visible spectroscopy. N_2 isothermal adsorption–desorption test was used to obtain the specific surface area of the samples. An F-7000 spectrophotometer (Hitachi, Tokyo, Japan) was used to collect the room-temperature photoluminescence (PL) spectra of the samples.

2.3. Fabrication of Gas Sensors and Tests

The measuring electrode was fabricated on the basis of an alumina substrate (6 × 30 mm). The gear-shaped electrode had a width of 0.42 mm, with an inter-electrode gap of 0.42 mm between the adjacent gear-shaped electrodes. The samples were prepared for the gas-sensing studies using the following procedures: First, platinum sizing agent was printed on the alumina (Al_2O_3) substrate by using screen printing. The alumina matrixes were subsequently dried at 80 °C for 40 min. Subsequent calcination was performed at 350 °C and 850 °C for 20 min at each temperature. The $In_2O_3/Ti_3C_2T_x$ paste sensing materials were printed on the alumina matrix by using screen printing method. Finally, the as-products were annealed at 350 °C for 1 h under argon atmosphere to remove the organic solvent. According to our previous test result [30], the thickness of the gas-sensing film is about 4 μm.

This work mainly focuses on the enhancement of the gas-sensing performance of the $In_2O_3/Ti_3C_2T_x$ composite material, characterizing the morphology and chemical state of the composite, and studying and discussing the gas-sensing performance and mechanism. The gas-sensing performance of the sensor was evaluated using a commercial four-channel test system (SD101, Wuhan HuachuangRuike Tech. Co., Ltd., Wuhan, China). The testing apparatus includes three main components: a computer for data acquisition, a precision gas flow controller, and a multi-channel test chamber. All measurements were conducted at room temperature. For each test, the measuring electrode was placed in a closed chamber filled with air until a stable resistance baseline was established. Subsequently, target gases with different concentrations were introduced. A minimum of three identical samples were tested for each condition, and the average response values were calculated. The response value of the materials to NO_2 can be determined using the following equation:

$$\text{Response} = R_g/R_a$$

where R_a is the sample resistance in air, and R_g is the sample resistance in the presence of NO_2 gas.

3. Results and Discussion

3.1. Characterization

XRD patterns are presented in Figure 2a, the diffraction peak of Ti_3AlC_2 at 2θ = 9.63° corresponds to the (002) crystal plane [31]. After etching with HCl and LiF, the (002) peak shifts to a lower diffraction angle (from 2θ = 9.5° to 5.8°), and its intensity broadens. This shift indicates an increase in the interlayer spacing, consistent with selective removal of the Al atom layers [32]. These results confirm the successful synthesis of $Ti_3C_2T_x$. The diffraction peaks of In_2O_3 located at 2θ of 21.5°, 30.5°, 35.4°, and 51.0° and 60.6° correspond to the (211), (222), (400), (440), and (600) planes of In_2O_3 phase, respectively (JCPDS card No. 89-4595). Comparing the XRD patterns of the $In_2O_3/Ti_3C_2T_x$ composite with those of the pristine In_2O_3 and $Ti_3C_2T_x$, the XRD characteristic peaks of In_2O_3 and $Ti_3C_2T_x$ appear simultaneously in the $In_2O_3/Ti_3C_2T_x$, indicating the presence of In_2O_3 and $Ti_3C_2T_x$ in the composite.

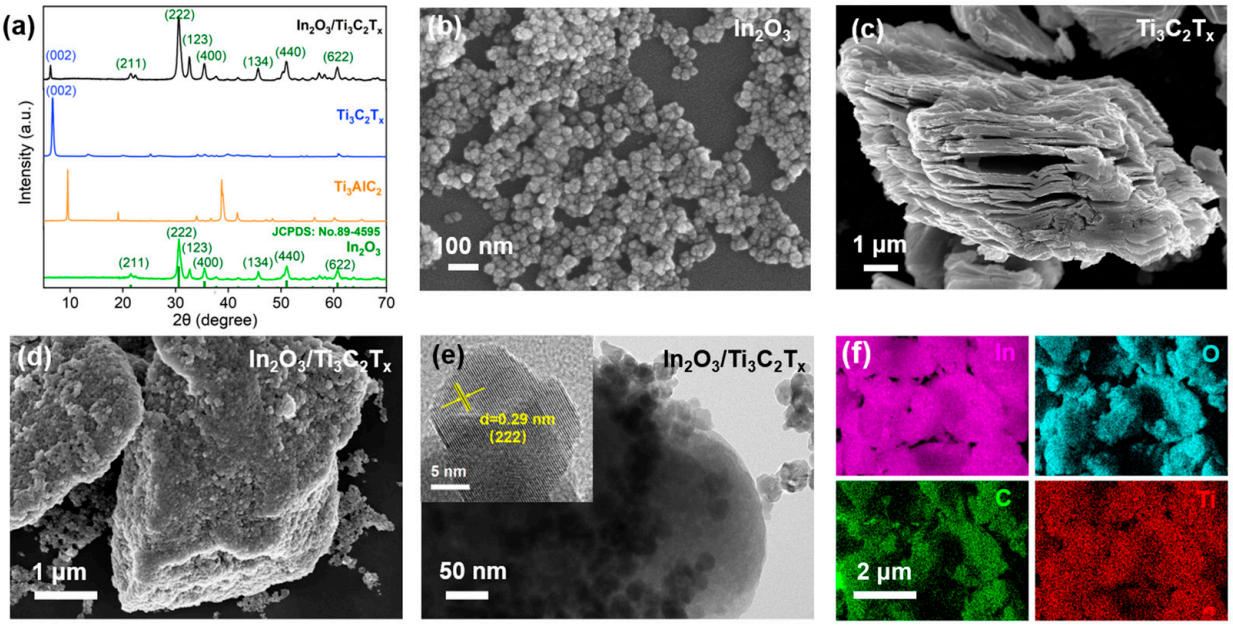


Figure 2. (**a**) XRD patterns of pristine In_2O_3 nanoparticles, Ti_3AlC_2, pristine $Ti_3C_2T_x$, and $In_2O_3/Ti_3C_2T_x$ composite; SEM images of (**b**) In_2O_3 nanoparticles, (**c**) $Ti_3C_2T_x$, and (**d**) $In_2O_3/Ti_3C_2T_x$ composite; (**e**) TEM and HRTEM images of $In_2O_3/Ti_3C_2T_x$; (**f**) EDS mapping analysis of In, O, C, and Ti elements in $In_2O_3/Ti_3C_2T_x$ composite.

SEM was employed to analyze the morphologies of pristine In_2O_3, $Ti_3C_2T_x$, and $In_2O_3/Ti_3C_2T_x$ composites. As shown in Figure 2b, the In_2O_3 nanoparticles exhibit consistent morphology and size distribution, with dense surface, good crystallinity, and uniform dispersion. Figure 2c illustrates that $Ti_3C_2T_x$ has a micron-scale size and presents an accordion-like multilayer nanosheet structure. This indicates that the Al atom layer in the Ti_3AlC_2 precursor structure is selectively etched, resulting in a typical 2D layered structure, which makes it possible for In_2O_3 nanoparticles to be inserted into deep regions of $Ti_3C_2T_x$. Figure 2d reveals that numerous In_2O_3 nanoparticles are attached to the surface of $Ti_3C_2T_x$, and some In_2O_3 nanoparticles penetrate into the gaps between the layers of $Ti_3C_2T_x$. This structure creates favorable conditions for the formation of heterojunction, which enhances the adsorption and diffusion of gas molecules on the surface of the composite, thereby pro-

moting the gas-sensitive performances of the $In_2O_3/Ti_3C_2T_x$ composite sensor. Figure 2e presents TEM images of the $In_2O_3/Ti_3C_2T_x$ composite, confirming that In_2O_3 nanoparticles are attached to the surface of $Ti_3C_2T_x$, consistent with the SEM observations. The HRTEM image in inset shows a lattice fringe spacing of 0.29 nm, corresponding to the (222) planes of In_2O_3, agreement with the XRD pattern. This confirms the favorable crystallinity of the $In_2O_3/Ti_3C_2T_x$ composite. EDS was employed to further confirm the elemental distribution and contents in the $In_2O_3/Ti_3C_2T_x$ composite materials. Figure 2f demonstrates a uniform distribution of In, O, C, and Ti elements, further illustrating the successful incorporation of In_2O_3 into the $Ti_3C_2T_x$ structure.

XPS analysis was applied to confirm the chemical states and elemental compositions in the $In_2O_3/Ti_3C_2T_x$ composite. In Figure 3a, the spectral peak of C 1s are located at 282.6 eV, 284.5 eV, 286.2 eV, and 288.3 eV, respectively, belonging to the C-Ti, C-C, C-O, and C-F bonds [33]. As shown in Figure 3b, the Ti 2p peaks of $Ti_3C_2T_x$ located at 455.4 eV, 456.0 eV, 457.5 eV, and 459.1 eV can be attributed to Ti-C, Ti_xO_y, Ti-x, and TiO_2, respectively [34]. XPS analysis of the O 1s region (Figure 3c) exhibits three characteristic peaks at 529.9 eV, 531.4 eV, and 533.2 eV, corresponding to lattice oxygen (O_L), oxygen vacancy (O_V), and adsorbed oxygen (O_C), respectively. The O_C refers to the oxygen species bound on the material surface through physical or chemical actions. This oxygen may come from air exposure, surface reactions, or treatment processes. The O_L refers to the oxygen atoms in the crystal structure that are periodically arranged and occupy fixed lattice positions and combine with the metal ions inside the oxide. The O_V refers to point defects formed in crystalline materials due to the absence of oxygen atoms. The existence of oxygen vacancies can enhance the carrier transport rate, thereby improving the gas sensitivity performance. The oxidized Ti states observed in Ti 2p spectrum correlate with the O_L in O 1s spectrum of $In_2O_3/Ti_3C_2T_x$. Figure 3d shows the In 3d spectra of $In_2O_3/Ti_3C_2T_x$. The peaks of In 3d 5/2 and In 3d 3/2 are 444.4 eV and 452 eV, respectively, which are In-O bonds in In_2O_3, consistent with the presence of In^{3+} [35].

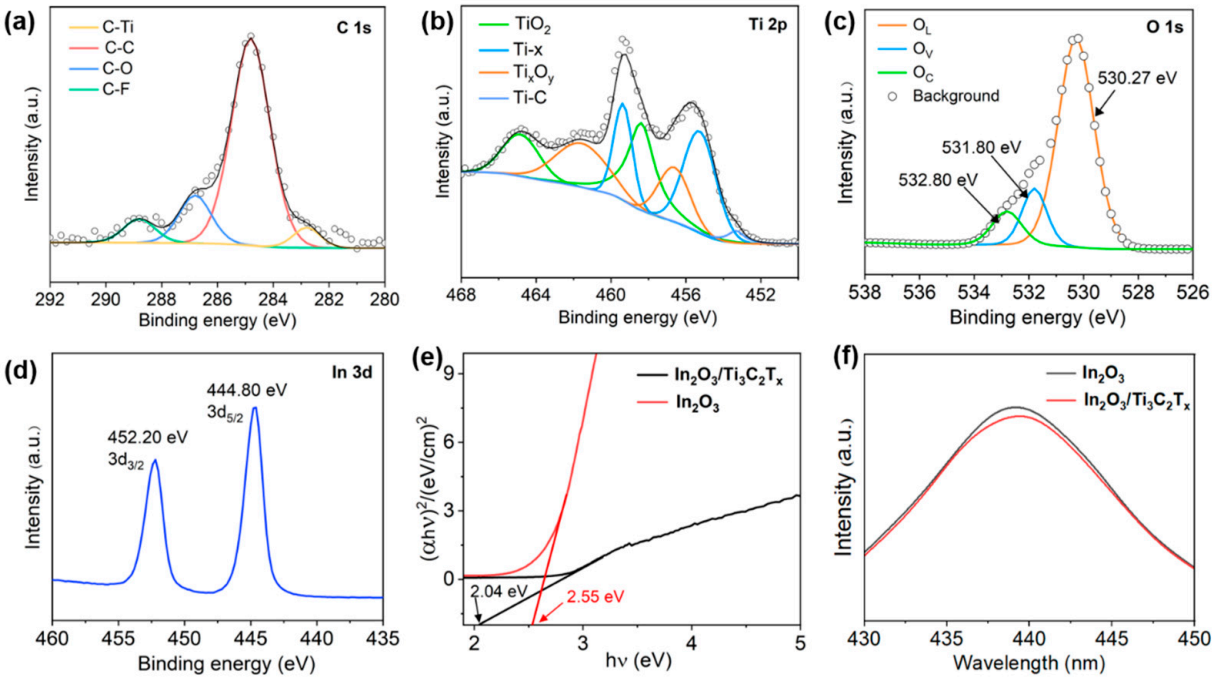


Figure 3. XPS spectra of $In_2O_3/Ti_3C_2T_x$ composite: (**a**) C 1s, (**b**) Ti 2p, (**c**) O 1s, and (**d**) In 3d; (**e**) Tauc plot and (**f**) PL spectra of In_2O_3 nanoparticles and $In_2O_3/Ti_3C_2T_x$ composite.

The band gap values of In_2O_3 and $In_2O_3/Ti_3C_2T_x$ are calculated to be 2.55 eV and 2.04 eV according to the Tauc plot (Figure 3e), respectively [36]. The narrower direct band gap of $In_2O_3/Ti_3C_2T_x$ indicates that less energy is required to excite electrons to the conduction band, which enhances the electron transfer rate. This observation further clarifies why the performance of the $In_2O_3/Ti_3C_2T_x$ composite is significantly better than that of pristine In_2O_3 nanoparticles [37]. As shown in Figure 3f, the photoluminescence intensity of the $In_2O_3/Ti_3C_2T_x$ composite is lower than that of the In_2O_3 nanoparticles. This effect originates from the interaction between $Ti_3C_2T_x$ and In_2O_3. Additionally, the reduced photoluminescence intensity suggests enhanced electron mobility in the $In_2O_3/Ti_3C_2T_x$ composite, which generally facilitates improved electron transport, thereby enhancing the gas-sensing performance of the sensor [38].

3.2. Gas-Sensing Performances

Figure 4a presents the response values of pristine In_2O_3, IT1, IT2, and IT3 to 100 ppm NO_2 at room temperature. The pristine In_2O_3 exhibits a relatively low response value of 7.9, while all composites demonstrate significantly enhanced responses. Notably, the IT2 composite achieves the maximum response value of 55.9. These results suggest that an optimal combination of $Ti_3C_2T_x$ enhances the gas-sensing performance of the sensors, while excessive $Ti_3C_2T_x$ will inhibit the responses. Figure 4b displays the resistance response curve of $In_2O_3/Ti_3C_2T_x$ sensor to 0.3–100 ppm NO_2, while the inserted image shows the response–recovery curve of the gas sensors to 0.3 ppm NO_2. The response value increases with the increase of NO_2 concentration. It is clearly seen that the response curve exhibits an increase in resistance followed by its decrease, particularly for 100 ppm NO_2. We propose the following several possibilities: (i) Fluctuations in airflow during the flow-switching process of the test equipment. At the moment when the gas flow rate switches, the actual gas flow rate may be higher than the actual set value for an instant. At this time, the resistance changes significantly. As the gas flow rate drops to a stable state, the resistance value gradually decreases. (ii) When the test gas is switched from air to NO_2, the gas has not yet fully filled the test chamber. At this stage, the gas diffusion rate is relatively high, and the gas-sensitive reaction is intense, leading to a significant increase in resistance. As NO_2 gradually fills the chamber, the diffusion rate decreases, and the gas-sensitive reaction process becomes less intense, resulting in a gradual reduction in the amplitude of resistance change. The logarithmic linear fitting curves of In_2O_3 and $In_2O_3/Ti_3C_2T_x$ gas sensors are shown in Figure 4c, where the response value data of the pristine In_2O_3 to different concentrations of NO_2 at room temperature are derived from previously published papers [39]. Compared with In_2O_3 gas sensor, $In_2O_3/Ti_3C_2T_x$ sensor shows a sensitivity of 0.86 with a linearity of $R^2 = 0.98$. Figure 4d displays the response/recovery time of the $In_2O_3/Ti_3C_2T_x$ composite gas sensor to 25 ppm NO_2, the calculation results show that the response/recovery times are 198/94 s. According to our previous study [39], the resistance of pure In_2O_3 is approximately 100 kΩ. The addition of $Ti_3C_2T_x$ reduces the resistance of the composite gas sensor to 2 kΩ. This remarkable reduction in resistance originates from the excellent electrical conductivity of $Ti_3C_2T_x$, which facilitates efficient electron transport when combined with In_2O_3, ultimately leading to the observed reduction in overall composite resistance.

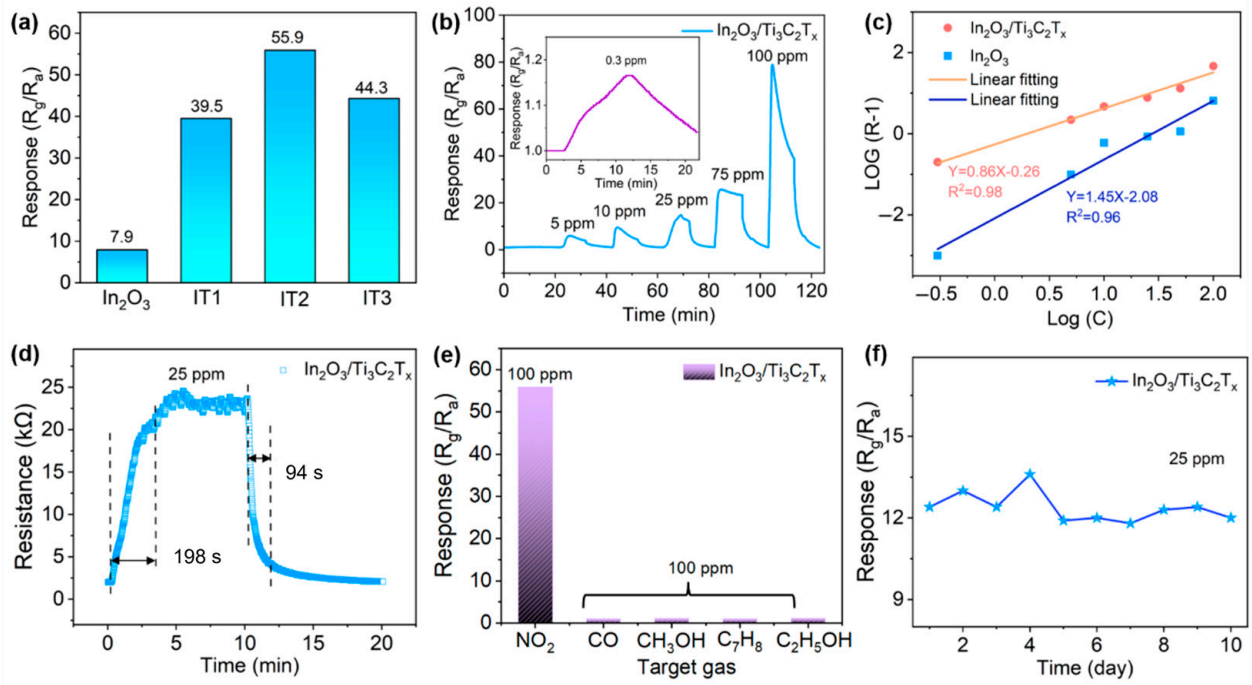


Figure 4. (**a**) Response values of $In_2O_3/Ti_3C_2T_x$ sensors with different contents to 100 ppm NO_2 at room temperature; (**b**) dynamic response/recovery curves of the $In_2O_3/Ti_3C_2T_x$ gas sensor to 0.3–100 ppm NO_2 at room temperature; (**c**) logarithmic linear fitting curves of In_2O_3 [31] and $In_2O_3/Ti_3C_2T_x$ composite gas sensors; (**d**) amplified response curve of $In_2O_3/Ti_3C_2T_x$ gas sensor to 25 ppm NO_2; (**e**) selective responses for the $In_2O_3/Ti_3C_2T_x$ gas sensor to various gases; (**f**) responses of the $In_2O_3/Ti_3C_2T_x$ gas sensor to 25 ppm NO_2 in 10 days.

To assess the impact of different gas selectivity on sensor performance in complex environments, the response performance of $In_2O_3/Ti_3C_2T_x$ composite sensor to carbon monoxide (CO), methanol (CH_3OH), ethanol (C_2H_5OH), and toluene (C_7H_8) are also tested at room temperature. The response value of the materials to the above four gases can be determined using the following equation:

$$\text{Response} = R_a/R_g$$

where R_a is the sample resistance in air, and R_g is the sample resistance in the presence of CO, CH_3OH, C_2H_5OH, or C_7H_8 gas. Figure 4e shows the response of the $In_2O_3/Ti_3C_2T_x$ sensor to 100 ppm of each of the four gases at room temperature. The response values for CO, CH_3OH, C_7H_8, and C_2H_5OH gases are 1, 1.1, 1.2, and 1, respectively. Obviously, the response value of the $In_2O_3/Ti_3C_2T_x$ composite sensor to NO_2 is significantly higher than that of the other gases. The gas-sensing performance of the $In_2O_3/Ti_3C_2T_x$ composite was tested once a day for ten consecutive days at room temperature. Figure 4f demonstrates that the response of the $In_2O_3/Ti_3C_2T_x$ gas sensor to NO_2 exhibits a fluctuation with an absolute deviation of 6.8% over a 10-day period, indicating that it has good stability. Although the humidity-related NO_2 sensing performances have not been tested, it is speculated, based on existing studies, that humidity interference will reduce the NO_2 sensing performances [40–43]. As shown in Table 1 [40,44–47], the proposed $In_2O_3/Ti_3C_2T_x$ sensor is competitive compared with the previously reported oxide-based NO_2 gas sensors in terms of working temperature and response value. Therefore, the $In_2O_3/Ti_3C_2T_x$ can be a highly responsive and selective sensing material for practical NO_2 sensors.

Table 1. Comparisons of the proposed $In_2O_3/Ti_3C_2T_x$ NO_2 sensor with the reports NO_2 sensors.

Materials	Working Temperature (°C)	Response (Resistance Ratio)	Detection Range (ppm)	Selectivity Ratio	Ref.
In_2O_3 micro flower	125	19.6 (5ppm)	-	~21.7	[44]
Pt decorated In_2O_3	300	11 (200 ppm)	-	~11.2	[45]
$VS_2/Ti_3C_2T_x/TiO_2$ nanocomposites	180	4.73 (50 ppm)	10–50	-	[40]
ZnO nanorod	150	6.7 (100 ppm)	-	~12.4	[46]
WO_3 Nanorod	200	24 (100 ppm)	-	~15.6	[47]
$In_2O_3/Ti_3C_2T_x$	Room temperature	55 (100 ppm)	0.3–100	45.8	This work

3.3. Gas-Sensing Mechanism

The sensing mechanism of the $In_2O_3/Ti_3C_2T_x$ composite is exhibited in Figure 5a. The detection mechanism for NO_2 in semiconductors is based on changes in surface resistance. Upon exposure to air, a large number of O_2 molecules are adsorbed onto the surface of the $In_2O_3/Ti_3C_2T_x$ composite, resulting in the formation of chemisorbed oxygen (O_2^-). This process leads to the development of an electron depletion layer. Once the oxidizing NO_2 gas interacts with the surface of the $In_2O_3/Ti_3C_2T_x$, it reacts with the e^-, forming NO_2^- ($NO_2 + e^- \rightarrow NO_2^-$), and continues to extract electrons from the $In_2O_3/Ti_3C_2T_x$, thereby causing the electron depletion layer to expand. In this process, the transfer of electrons is hindered, the electron mobility is reduced, and the resistance of the material is increased [37].

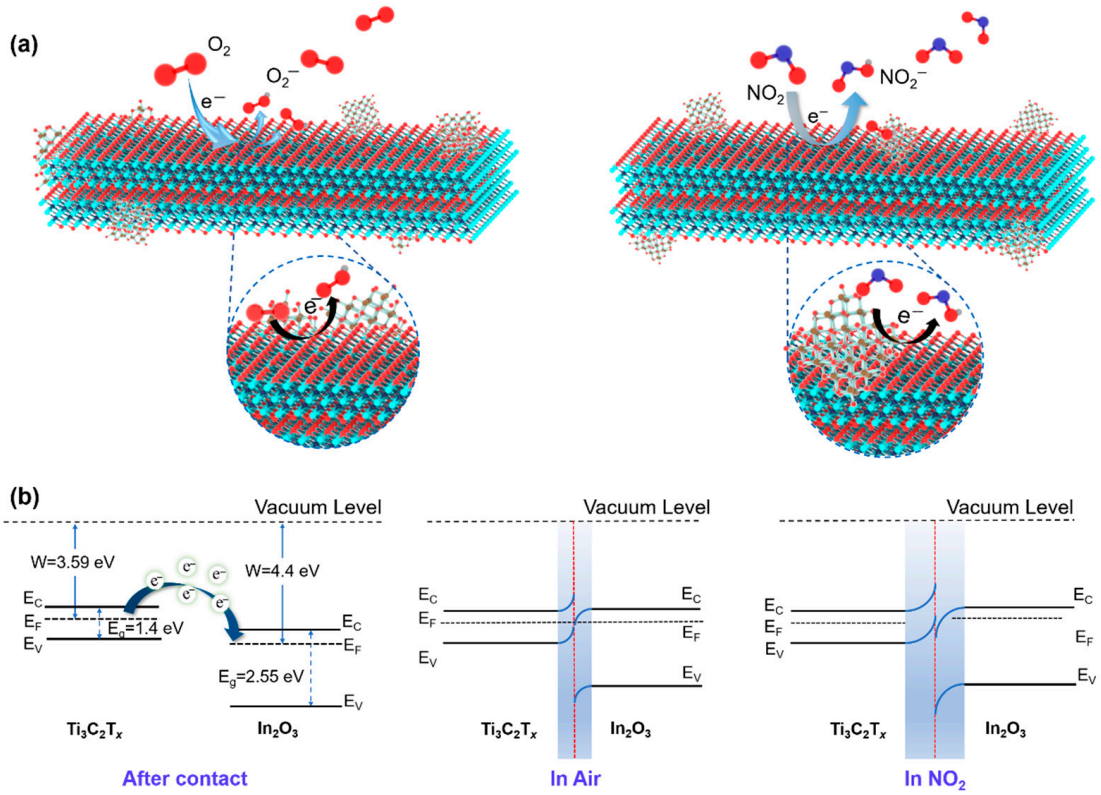


Figure 5. (**a**) Schematic illustration of the sensing mechanism of the $In_2O_3/Ti_3C_2T_x$ composite; (**b**) energy band structure of $In_2O_3/Ti_3C_2T_x$ composite in air and NO_2 atmospheres.

Figure 5b shows the band structure diagram of the $In_2O_3/Ti_3C_2T_x$ composite. The work function and band gap of In_2O_3 and $Ti_3C_2T_x$ are W_f = 4.4 eV and 3.59 eV, E_g = 2.55 eV and 1.4 eV, respectively [48]. When In_2O_3 and $Ti_3C_2T_x$ make contact, a heterojunction is formed, improving the activity of the charge transfer, which further enhances the gas-sensing properties of the composite. To achieve Fermi-level equilibrium, the energy band of In_2O_3 and $Ti_3C_2T_x$ bend, which cause the electrons to move from $Ti_3C_2T_x$ to In_2O_3. As a result of this electron transfer, an electron depletion layer is established at the interface of In_2O_3 to $Ti_3C_2T_x$. In NO_2, the depletion region widens after the adsorbed gas molecules capture electrons, the free-moving electrons in n-type $In_2O_3/Ti_3C_2T_x$ reducing, thereby increasing the $In_2O_3/Ti_3C_2T_x$ sensor resistance.

4. Conclusions

In this study, the $In_2O_3/Ti_3C_2T_x$ composites were successfully synthesized through a facile electrostatic self-assembly method. The gas-sensing properties of the $In_2O_3/Ti_3C_2T_x$ NO_2 sensor were investigated at room temperature. The $In_2O_3/Ti_3C_2T_x$ composite containing 2% $Ti_3C_2T_x$ exhibited the best NO_2 sensing performance with a response value of 55.9, and fast response and recovery (198 s and 94 s). Finally, a NO_2 sensing mechanism of a $In_2O_3/Ti_3C_2T_x$ gas sensor is constructed based on p-n heterojunction enhancement and molecular adsorption. This work provides a new way for a rational design of MXene-based gas sensors, and further demonstrates a pathway for the systematic development of NO_2-sensing materials.

Author Contributions: Conceptualization, Z.Z., Q.Z., L.Y. and Y.X.; methodology, Y.G., H.F. and Z.Z.; validation, Y.G., H.F. and Z.Z.; formal analysis, H.F., Q.D., Z.D. and M.H.; investigation, H.F., Z.Z. and Y.X.; data curation, Y.G., H.F., Z.Z., Q.D. and S.G.; writing—original draft preparation, Y.G.; writing—review and editing, Q.Z., Z.D., M.H. and Y.X.; supervision, L.Y.; project administration, L.Y. and S.G.; funding acquisition, L.Y. and S.G. All authors have read and agreed to the published version of the manuscript.

Funding: This work is supported by Yunnan Fundamental Research Projects (grant NO. 202401BE070001-005, 202501CF070183, 202401BE070001-021), the Natural Science Foundation of China (grant NO. 52364051, 52304400, 62101225, 22368029), Central Guidance Local Scientific and Technological Development Funds (grant NO. 202407AB110022), Yunnan Major Scientific and Technological Projects (No. 202302AG050002), the Key Technology Research and Development Program of Shandong Province (No. 2023CXGC010903), the open project (KJS2306) of Jiangsu Key Laboratory for Carbon-Based Functional Materials and Devices, Soochow University and Central guidance local scientific and technological development funds (202407AB110022). The authors (Shenghui Guo, Yunling Scholar; Li Yang, Industrial Innovation Scholar) would like to acknowledge the Yunnan Province Xingdian Talent Support Plan Project.

Institutional Review Board Statement: Not applicable.

Informed Consent Statement: Not applicable.

Data Availability Statement: Data is contained within this article.

Conflicts of Interest: The authors declare no conflicts of interest.

References

1. Bhowmick, T.; Ghosh, A.; Nag, S.; Majumder, S. Sensitive and selective CO_2 gas sensor based on CuO/ZnO bilayer thin-film architecture. *J. Alloys Compd.* **2022**, *903*, 163871. [CrossRef]
2. Keerthana, S.; Rathnakannan, K. Hierarchical ZnO/CuO nanostructures for room temperature detection of carbon dioxide. *J. Alloys Compd.* **2022**, *897*, 162988. [CrossRef]
3. Ji, H.; Guo, S.; Gao, L.; Yang, L.; Yan, H.; Zeng, H. Revolutionizing titanium production: A comprehensive review of thermochemical and molten salt electrolysis processes. *Int. J. Min. Met. Mater.* **2025**. [CrossRef]

4. Qian, Y.; Li, H.; Rosenberg, A.; Li, Q.; Sarnat, J.; Papatheodorou, S.; Schwartz, J.; Liang, D.; Liu, Y.; Liu, P. Long-term exposure to low-level NO_2 and mortality among the elderly population in the southeastern United States. *Environ. Health Perspect.* **2021**, *129*, 127009. [CrossRef] [PubMed]
5. Li, Q.; Zeng, W.; Li, Y. Metal oxide gas sensors for detecting NO_2 in industrial exhaust gas: Recent developments. *Sens. Actuators B Chem.* **2022**, *359*, 131579. [CrossRef]
6. Wu, P.; Qiu, X.; Wu, Y.; Duan, Z.; Ma, Y.; Yu, H.; Yuan, Z.; Jiang, Y.; Tai, H. Linear Model for Concentration Measurement of Mixed Gases. *ACS Sens.* **2025**, *10*, 1948–1958. [CrossRef] [PubMed]
7. Yuan, Z.; Zhao, Q.; Duan, Z.; Xie, C.; Duan, X.; Li, S.; Ye, Z.; Jiang, Y.; Tai, H. Ag_2Te nanowires for humidity-resistant trace-level NO_2 detection at room temperature. *Sens. Actuators B Chem.* **2022**, *363*, 131790. [CrossRef]
8. Liu, S.; Wang, M.; Ge, C.; Lei, S.; Hussain, S.; Wang, M.; Qiao, G.; Liu, G. Enhanced room-temperature NO_2 sensing performance of SnO_2/Ti_3C_2 composite with double heterojunctions by controlling co-exposed {221} and {110} facets of SnO_2. *Sens. Actuators B Chem.* **2022**, *365*, 131919. [CrossRef]
9. Sun, Z.; Yan, X.; Huang, L.; Zhang, Y.; Hu, Z.; Sun, C.; Yang, X.; Pan, G.; Cheng, Y. AuPd bimetallic functionalized monodisperse In_2O_3 porous spheres for ultrasensitive trimethylamine detection. *Sens. Actuators B Chem.* **2023**, *381*, 133355. [CrossRef]
10. Yang, R.; Yuan, Z.; Jiang, C.; Zhang, X.; Qiao, Z.; Zhang, J.; Liang, J.; Wang, S.; Duan, Z.; Wu, Y. Ultrafast Hydrogen Detection System Using Vertical Thermal Conduction Structure and Neural Network Prediction Algorithm Based on Sensor Response Process. *ACS Sens.* **2025**, *10*, 2181–2190. [CrossRef]
11. Bonardo, D.; Septiani, N.L.W.; Amri, F.; Humaidi, S.; Yuliarto, B. Recent development of WO_3 for toxic gas sensors applications. *J. Electrochem. Soc.* **2021**, *168*, 107502. [CrossRef]
12. Sun, K.; Zhan, G.; Zhang, L.; Wang, Z.; Lin, S. Highly sensitive NO_2 gas sensor based on ZnO nanoarray modulated by oxygen vacancy with Ce doping. *Sens. Actuators B Chem.* **2023**, *379*, 133294. [CrossRef]
13. Duan, X.; Jiang, Y.; Liu, B.; Duan, Z.; Zhang, Y.; Yuan, Z.; Tai, H. Enhancing the carbon dioxide sensing performance of LaFeO3 by Co doping. *Sens. Actuators B Chem* **2024**, *402*, 135136. [CrossRef]
14. Zhang, Y.H.; Liu, Y.C.; Liu, J.L.; Qu, Z.H.; Tian, S.Y.; Liu, H. Anti-humidity and high sensitivity sensor for detecting acetone with Ce-ZnO nanosheets. *Ceram. Int.* **2024**, *50*, 29787–29798. [CrossRef]
15. Meghana, N.; Zimba, V.; Nayak, J. Enhancement of room temperature sensitivity and reduction of baseline drift in $WO_3/g\text{-}C_3N_4$ nanocomposite based volatile organic compound gas sensors. *Ceram. Int.* **2025**, *51*, 6233–6243.
16. Liu, X.C.; Wang, J.H.; Zhang, Y.T.; Zhang, D.Z. Hydrogen sulfide gas sensing characteristics based on copper oxide/molybdenum diselenide heterojunction. *J. Alloys Compd.* **2023**, *963*, 171197. [CrossRef]
17. Pinna, N.; Neri, G.; Antonietti, M.; Niederberger, M. Nonaqueous synthesis of nanocrystalline semiconducting metal oxides for gas sensing. *Angew. Chem. Int. Ed.* **2004**, *43*, 4345–4349. [CrossRef] [PubMed]
18. Waitz, T.; Wagner, T.; Sauerwald, T.; Kohl, C.D.; Tiemann, M. Ordered mesoporous In_2O_3: Synthesis by structure replication and application as a methane gas sensor. *Adv. Funct. Mater.* **2009**, *19*, 653–661. [CrossRef]
19. Zhang, B.; Bao, N.; Wang, T.; Xu, Y.; Dong, Y.; Ni, Y.; Yu, P.; Wei, Q.; Wang, J.; Guo, L. High-performance room temperature NO_2 gas sensor based on visible light irradiated In_2O_3 nanowires. *J. Alloys Compd.* **2021**, *867*, 159076. [CrossRef]
20. Chen, X.; Shen, Y.; Zhang, W.; Zhang, J.; Wei, D.; Lu, R.; Zhu, L.; Li, H.; Shen, Y. In-situ growth of ZnO nanowire arrays on the sensing electrode via a facile hydrothermal route for high-performance NO_2 sensor. *Appl. Surf. Sci.* **2018**, *435*, 1096–1104. [CrossRef]
21. Zheng, S.; Sun, J.; Hao, J.; Sun, Q.; Wan, P.; Li, Y.; Zhou, X.; Yuan, Y.; Zhang, X.; Wang, Y. Engineering SnO_2 nanorods/ethylenediamine-modified graphene heterojunctions with selective adsorption and electronic structure modulation for ultrasensitive room-temperature NO_2 detection. *Nanotechnology* **2021**, *32*, 155505. [CrossRef]
22. Zhao, Q.-N.; Zhang, Y.-J.; Duan, Z.-H.; Wang, S.; Liu, C.; Jiang, Y.-D.; Tai, H.-L. A review on $Ti_3C_2T_x$-based nanomaterials: Synthesis and applications in gas and humidity sensors. *Rare Met.* **2021**, *40*, 1459–1476. [CrossRef]
23. Gogotsi, Y.; Anasori, B. The rise of MXenes. In *MXenes*; Jenny Stanford Publishing: New York, NY, USA, 2023; pp. 3–11.
24. Xu, B.; Gogotsi, Y. MXenes-The fastest growing materials family in the two-dimensional world. *Chin. Chem. Lett.* **2020**, *31*, 919–921. [CrossRef]
25. Naguib, M.; Mashtalir, O.; Carle, J.; Presser, V.; Lu, J.; Hultman, L.; Gogotsi, Y.; Barsoum, M.W. Two-dimensional transition metal carbides. *ACS Nano* **2012**, *6*, 1322–1331. [CrossRef] [PubMed]
26. Choi, J.-M.; Byun, J.-H.; Kim, S.S. Influence of grain size on gas-sensing properties of chemiresistive p-type NiO nanofibers. *Sens. Actuators B Chem.* **2016**, *227*, 149–156. [CrossRef]
27. Zhang, J.; Liu, X.; Neri, G.; Pinna, N. Nanostructured materials for room-temperature gas sensors. *Adv. Mater.* **2016**, *28*, 795–831. [CrossRef]
28. Ta, Q.T.H.; Sreedhar, A.; Tri, N.N.; Noh, J.-S. In situ growth of TiO_2 on $Ti_3C_2T_x$ MXene for improved gas-sensing performances. *Ceram. Int.* **2024**, *50*, 27227–27236. [CrossRef]

29. Liu, S.; Wang, M.; Liu, G.; Wan, N.; Ge, C.; Hussain, S.; Meng, H.; Wang, M.; Qiao, G. Enhanced NO_2 gas-sensing performance of 2D Ti_3C_2/TiO_2 nanocomposites by in-situ formation of Schottky barrier. *Appl. Surf. Sci.* **2021**, *567*, 150747. [CrossRef]
30. Zhang, D.; Du, Q.; Yang, L.; Gao, J.; Yi, J.; Hou, M.; Guo, S.; Zeng, H. High-Throughput Experimental Technology: Rapid Identification of the Precious Metal Modified In 2 O 3 for NO 2 Low-Temperature Sensing. *IEEE Sens. J.* **2023**, *23*, 8101–8108. [CrossRef]
31. Maleski, K.; Shuck, C.E.; Fafarman, A.T.; Gogotsi, Y. The broad chromatic range of two-dimensional transition metal carbides. *Adv. Opt. Mater* **2021**, *9*, 2001563. [CrossRef]
32. Peng, M.; Wang, L.; Li, L.; Tang, X.; Huang, B.; Hu, T.; Yuan, K.; Chen, Y. Manipulating the interlayer spacing of 3D MXenes with improved stability and zinc-ion storage capability. *Adv. Funct. Mater.* **2022**, *32*, 2109524. [CrossRef]
33. Zhao, Q.; Zhou, W.; Zhang, M.; Wang, Y.; Duan, Z.; Tan, C.; Liu, B.; Ouyang, F.; Yuan, Z.; Tai, H. Edge-enriched $Mo_2TiC_2T_x/MoS_2$ heterostructure with coupling interface for selective NO_2 monitoring. *Adv. Funct. Mater.* **2022**, *32*, 2203528. [CrossRef]
34. Yang, E.; Park, K.H.; Oh, T.; Kim, S.J. Ultra-dense SnO_2 QDs-decorated MXene nanosheets with high water dispersibility for rapid NH_3 sensing at room temperature. *Sens. Actuators B Chem.* **2024**, *409*, 135542. [CrossRef]
35. Qin, W.; Lu, B.; Xu, X.; Shen, Y.; Meng, F. Metal organic framework-derived porous Ni-doped In_2O_3 for highly sensitive and selective detection to hydrogen at low temperature. *Sens. Actuators B Chem.* **2024**, *417*, 136123. [CrossRef]
36. Xia, Y.; Le, T.; Peng, J.; Ravindra, A.; Xu, L. Pt quantum dots decorated nest-like 3D porous ZnO nanostructures for enhanced visible-light degradation of RhB. *J. Porous Mater.* **2020**, *27*, 1339–1348. [CrossRef]
37. Bai, X.; Lv, H.; Liu, Z.; Chen, J.; Wang, J.; Sun, B.; Zhang, Y.; Wang, R.; Shi, K. Thin-layered MoS_2 nanoflakes vertically grown on SnO_2 nanotubes as highly effective room-temperature NO_2 gas sensor. *J. Hazard. Mater.* **2021**, *416*, 125830. [CrossRef]
38. Chen, Q.; Liu, Y.; Gu, X.; Li, D.; Zhang, D.; Zhang, D.; Huang, H.; Mao, B.; Kang, Z.; Shi, W. Carbon dots mediated charge sinking effect for boosting hydrogen evolution in Cu-In-Zn-S QDs/MoS_2 photocatalysts. *Appl. Catal. B-Environ.* **2022**, *301*, 120755. [CrossRef]
39. Xiang, J.C.; Zhang, Z.X.; Li, X.; Yang, L.; Guo, S.H.; Xia, Y. In_2O_3/MoS_2 composite prepared by electrostatic self-assembly for NO_2 sensing at room-temperature. *J. Porous Mater.* **2025**, *5*, 1–10. [CrossRef]
40. Zhao, Z.; Tian, J.; Xu, X.; Zheng, C.; Wu, L. Highly sensitive NO_2 gas sensor based on $VS_2/Ti_3C_2T_x/TiO_2$ nanocomposites. *Microchem. J.* **2025**, *212*, 113563. [CrossRef]
41. Yao, Y.; Wang, Z.; Han, Y.; Xie, L.; Zhao, X.; Shahrokhian, S.; Barsan, N.; Zhu, Z. Conductometric $Cr_2O_3/TiO_2/Ti_3C_2T_x$ gas sensor for detecting triethylamine at room temperature. *Sens. Actuators B* **2023**, *381*, 133412. [CrossRef]
42. Qiu, L.; Huo, Y.; Pan, Z.; Wang, T.; Yu, H.; Liu, X.; Tong, X.; Yang, Y. Resister-type sensors based on $Ti_3C_2T_x$ MXene decorated In_2O_3 p-n heterojunction for ppb-level NO_2 detection at room temperature. *J. Environ. Chem. Eng* **2025**, *13*, 115249. [CrossRef]
43. Liu, M.; Ji, J.; Song, P.; Wang, J.; Wang, Q. Sensing performance of α-$Fe_2O_3/Ti_3C_2T_x$ MXene nanocomposites to NH_3 at room temperature. *J. Alloys Compd.* **2022**, *898*, 162812. [CrossRef]
44. Xiao, B.X.; Wang, D.X.; Song, S.L.; Zhai, C.B.; Wang, F.; Zhang, M.Z. Fabrication of mesoporous In_2O_3 nanospheres and their ultrasensitive NO_2 sensing properties. *Sens. Actuators B Chem.* **2017**, *248*, 519–526. [CrossRef]
45. Choi, S.B.; Lee, J.K.; Lee, W.S.; Ko, T.G.; Lee, C. Optimization of the Pt Nanoparticle Size and Calcination Temperature for Enhanced Sensing Performance of Pt-Decorated In_2O_3 Nanorods. *J. Korean Phys. Soc.* **2018**, *73*, 1444–1451. [CrossRef]
46. Vanalakar, S.A.; Gang, M.G.; Patil, V.L.; Dongale, T.D.; Patil, P.S.; Kim, J.H. Enhanced Gas-Sensing Response of Zinc Oxide Nanorods Synthesized via Hydrothermal Route for Nitrogen Dioxide Gas. *J. Electron. Mater.* **2019**, *48*, 589–595. [CrossRef]
47. Mulik, R.; Chougule, M.; Khuspe, G.; Patil, V. In Hydrothermal Synthesis of Tungsten Oxide for the Detection of NO_2 Gas. *Tec. Soc. Appl.* **2020**, *1*, 957–961.
48. Liu, M.; Song, P.; Yang, Z.; Wang, Q. MXene/In_2O_3 nanocomposites for formaldehyde detection at low temperature. *Inorg. Chem. Commun.* **2023**, *148*, 110302. [CrossRef]

Disclaimer/Publisher's Note: The statements, opinions and data contained in all publications are solely those of the individual author(s) and contributor(s) and not of MDPI and/or the editor(s). MDPI and/or the editor(s) disclaim responsibility for any injury to people or property resulting from any ideas, methods, instructions or products referred to in the content.